



# Organic-acid-directed assembly of iron–carbon oxides nanoparticles on coordinatively unsaturated metal sites of MIL-101 for green photochemical oxidation



Lei Qin<sup>a</sup>, Zhaowen Li<sup>a</sup>, Zehai Xu<sup>a</sup>, Xinwen Guo<sup>b</sup>, Guoliang Zhang<sup>a,\*</sup>

<sup>a</sup> Institute of Oceanic and Environmental Chemical Engineering, College of Chemical Engineering and Material Science and College of Ocean, Zhejiang University of Technology, Hangzhou 310014, China

<sup>b</sup> State Key Laboratory of Fine Chemicals, Department of Catalysis Chemistry and Engineering, Dalian University of Technology, Dalian 116012, China

## ARTICLE INFO

### Article history:

Received 7 April 2015

Received in revised form 30 May 2015

Accepted 1 June 2015

Available online 3 June 2015

### Keywords:

Metal organic frameworks (MOFs)

Organic-acid-directed approach

Iron–carbon oxide nanoparticles

Unsaturated metal sites

Synergistic effect

## ABSTRACT

Through a simple organic-acid-directed approach, *in situ* growth of iron–carbon oxide nanoparticles (NPs) were assembled on the coordinatively unsaturated Cr sites (CUSs) of MIL-101 and inserted into its cavities orderly for the first time. When citric acid was employed, the incorporation of more small NPs within the cage of metal organic frameworks (MOFs) without agglomeration on external surface can easily be achieved compared with traditional solution infiltration method, and the intact morphology structure, high crystallinity and porosity were remained for MIL-101 after supporting. The provided strategy was helpful to rational design of well dispersed metal-based NPs by enhancing the interaction between metal precursor and MOFs. Experimental results showed that Fe–C oxides immobilized to MIL-101 in the presence of citric acid or tartaric acid had remarkable catalytic activity for visible-light assisted Fenton reaction at neutral pH and possessed excellent tolerance for organic pollutant poisoning. Compared with other supports, such as TiO<sub>2</sub>, clays, mesoporous NH<sub>2</sub>–SiO<sub>2</sub> and MIL-53(Cr), the MIL-101 supported catalyst exhibited higher activity for activation of hydrogen peroxide, which was attributed to the unique structure/properties of support and favorable synergistic effect of [Fe–O–C] sites and Cr nodes of MIL-101. The progress will bring valuable insights to develop high-performance heterogeneous catalysts for the green photocatalytic oxidation and environmental remediation.

© 2015 Elsevier B.V. All rights reserved.

## 1. Introduction

Catalytic hydrogen peroxide oxidation (CHPO), as a green, inexpensive, and practical technology, exhibits valuable application for the degradation of toxic and refractory organic contaminants, such as pesticides, dyes, and pharmaceuticals [1,2]. The search for effi-

cient and stable catalyst still remains a great challenge for the wide application of CHPO to water purification. Recently, iron oxide supported on zeolite, mesoporous silica, clays, and TiO<sub>2</sub> materials for CHPO reaction guided us toward a highly promising alternative due to its abundance, low price and no toxicity [3–6]. However, the catalytic oxidation performance is far from ideal in comparison with noble metals [7,8]. Hence, the development of higher-performance support for the preparation of heterogeneous catalysts is of great importance.

Porous MOFs, a class of very promising hybrid functional materials, are currently being intensively investigated in the fields of gas storage, separation, sensing, and catalysis [9–12]. Over the past decades, although researchers have mostly focused on embedding noble monometal, bimetallic alloy or metal oxide (TiO<sub>2</sub>, ZnO, and PdO<sub>2</sub>) NPs into MOFs host framework for solid-state catalysis due to their exotic properties [13–17], such as high surface area and porosity, chemical tunability, and multi-functionality, there are currently few reports on embedding iron oxide NPs into MOFs for catalytic hydrogen peroxide oxidation [18]. One of the main difficulties is

**Abbreviations:** BET, Brunauer, Emmett, and Teller; CA, citric acid; CHPO, catalytic hydrogen peroxide oxidation; CUSs, coordinatively unsaturated metal sites; EDS, energy dispersive spectroscopy; Fe<sup>3+</sup>-CA/MIL-101(Cr) and Fe<sup>3+</sup>-TA/MIL-101(Cr), MIL-101(Cr) supporting with iron–carbon oxide nanoparticles; Fe<sup>3+</sup>/MIL-101(Cr), MIL-101(Cr) supporting with iron oxides nanoparticles; FTIR, Fourier transform infrared spectrophotometers; ICP, inductive coupled plasma emission spectrometer; MOFs, metal organic frameworks; NPs, nanoparticles; SEM, scanning electron microscope; SI, supporting information; SBU, secondary building units; TA, tartaric acid; TEM, transmission electron microscopy; TOC, total organic carbon; TEM, transmission electron microscopy; XPS, x-ray photoelectron spectroscopy; XRD, x-ray diffraction.

\* Corresponding author. Tel.: +86 571 88320863; fax: +86 571 88320863.

E-mail address: [guoliangz@zjut.edu.cn](mailto:guoliangz@zjut.edu.cn) (G. Zhang).

how to develop a rational method to load NPs inside the porous matrices of MOFs. Recently, methods including solution infiltration [14], solid grinding [19], microwave irradiation [20], and chemical vapor deposition [13] have been used to incorporate NPs into MOFs. However, the precursor compounds can frequently diffuse out through MOFs cavities to generate large NPs on external surface [21]. To overcome the difficulties, more efforts have been devoted to develop different strategies to confine and prevent the nucleation and growth of noble metal NPs on the surface, such as double solvents and “bottle around ship” methods [21–23]. Nevertheless, due to weak interaction between single iron active sites and MOFs, it seems difficult to completely prevent NPs agglomerating on the outer surface. Moreover, the adjustment of interaction and location between them is often critical to the activity. Therefore, it is essential for developing a general and facile method to strengthen the connection or interaction between Fe ions precursor and block building or ligand of MOFs.

Herein, we present a novel organic acid cooperative strategy to direct the incorporation of Fe–C oxides into MOFs cages, preventing the NPs aggregated on the outer surface of host matrix. Different with conventional solution impregnation, the adding of organic acid could significantly enhance the binding between metal ions and secondary building units (SBU) of MOFs, which can potentially be very useful in location and metal loading control. Moreover, simple organic molecules, such as organic acids and amino acids, are also reported to have advantage to increase the catalytic performance of heterogenous catalyst to oxidation of organic compounds in presence of  $H_2O_2$  [24,25]. To the best of our knowledge, there is currently no report on MOF-immobilized [Fe–O–C] sites with high activity in the decomposition of  $H_2O_2$  under the mild condition.

In this work, MIL-101(Cr) was selected as a host matrix for NPs nanoparticles supporting because of the following rationales: (1) the incredibly larger pore size (2.9–3.4 nm) and high specific surface area may facilitate the encapsulation of metal NPs inside the pores; (2) the significantly higher thermal- and hydro- stability in comparison with other MOFs makes it attractive for the wastewater treatment; (3) terminal water molecules of trimeric chromium (III) octahedral clusters are easy to be removed after vacuum treatment [26]. Due to these unique properties, when MIL-101(Cr) was immersed into metal-organic precursor, citric acid (CA) as a chelating agent established an interaction between iron ions and CUss of SBU through Coulombic attraction and coordination of electron-rich functional groups (Scheme 1). After low-temperature calcination, in situ growth of [Fe–O–C] sites was homogeneously anchored into the cage. However, in absence of CA, some iron oxides could generate on the external surface of support. The CA molecule played a location-directing role in incorporating NPs into the cavities of MOFs. More details of the effect of CA addition on the structure and activity of MIL-101 supported catalysts were investigated. Meanwhile, MIL-53(Cr),  $TiO_2$ , clays, and mesoporous  $NH_2-SiO_2$  were selected as supports to further explore the structure/properties-activity relationship and synergistic effect of active sites and support on the catalytic oxidation.

## 2. Experimental

### 2.1. Materials synthesis

#### 2.1.1. MIL-101(Cr)

According to the previous literature, MIL-101(Cr) was prepared by reacting terephthalic acid (332 mg, 2.0 mmol) with  $Cr(NO_3)_3 \cdot 9H_2O$  (800 mg, 2.0 mmol) in the presence of aqueous HF (2.0 mmol) and de-ionized water (9.5 mL) at 493 K for 8 h [26]. Microcrystalline green powders of MIL-101(Cr) with formula  $Cr_3F(H_2O)_2O[(O_2C)C_6H_4(CO_2)]_3 NH_2O$  ( $n \leq 25$ ) were produced dur-

ing the reaction. To eliminate the unreacted terephthalic acid, the crystalline MIL-101(Cr) product in the solution was doubly filtered off using two filters with pore sizes between 40 and 100  $\mu m$ , and then further purified by solvothermal treatment in ethanol at 353 K and washed with the hot ethanol. The resulting solid was finally dried overnight at 423 K under vacuum.

#### 2.1.2. MIL-53(Cr)

As previously reported, MIL-53(Cr) was hydrothermally synthesized from a mixture of  $Cr(NO_3)_3 \cdot 9H_2O$ , terephthalic acid, hydrofluoric acid (HF) (40%), and  $H_2O$  in the molar ratio 1:1:1:280 [27]. The resulting suspension was vigorously stirred and introduced in a Teflon-lined steel autoclave at 493 K for 3 days. In order to remove the unreacted organic ligand of pore and external surface, the as-synthesized MIL-53 was calcined at 523 K under air atmosphere.

#### 2.1.3. Mesoporous $NH_2-SiO_2$

As described by Wang et al., mesoporous  $NH_2-SiO_2$  were synthesized by anionic surfactant-templated method [28]. More details in the fabrication of mesoporous  $NH_2-SiO_2$  were presented in our previous work [6]. In a typical procedure, Sar-Na (0.5868 g), APES (0.25 mL) and TEOS (3.0 mL) were added to the mixture of deionized water and HCl solution (0.1 M), and then which was vigorously stirred. The obtained emulsion was transferred into Teflon-lined steel autoclave at 353 K for 24 h. After reaction, the surfactants in the as-synthesized solids were removed by an ion-exchange extraction method.

#### 2.1.4. $Fe^{3+}$ -CA/MIL-101(Cr)

In a typical synthesis, MIL-101(Cr) was activated at 423 K for 8 h under vacuum, and 100 mg of which was impregnated with the de-ionized water solution containing  $Fe(NO_3)_3 \cdot 9H_2O$  (metal ion/support = 10%, w/w) and citric acid (metal/CA = 1:1.5, mole ratio). The mixture was stirred at room temperature to form a homogeneous solution, and then transformed into the triangular flask and held at 333 K. The obtained powders were washed with distilled water and dried. And then the as-synthesized samples were treated in a stream of air at 473 K for 4 h to yield the MIL-101 supporting with iron–carbon oxides, denoted as  $Fe^{3+}$ -CA/MIL-101(Cr).

#### 2.1.5. $Fe^{3+}$ /MIL-101(Cr)

MIL-101 supported with iron oxides nanoparticles in absence of citric acid was also carried out similar to above procedure and the synthesized samples was denoted as  $Fe^{3+}$ /MIL-101(Cr).

#### 2.1.6. $Fe^{3+}$ -TA/MIL-101(Cr)

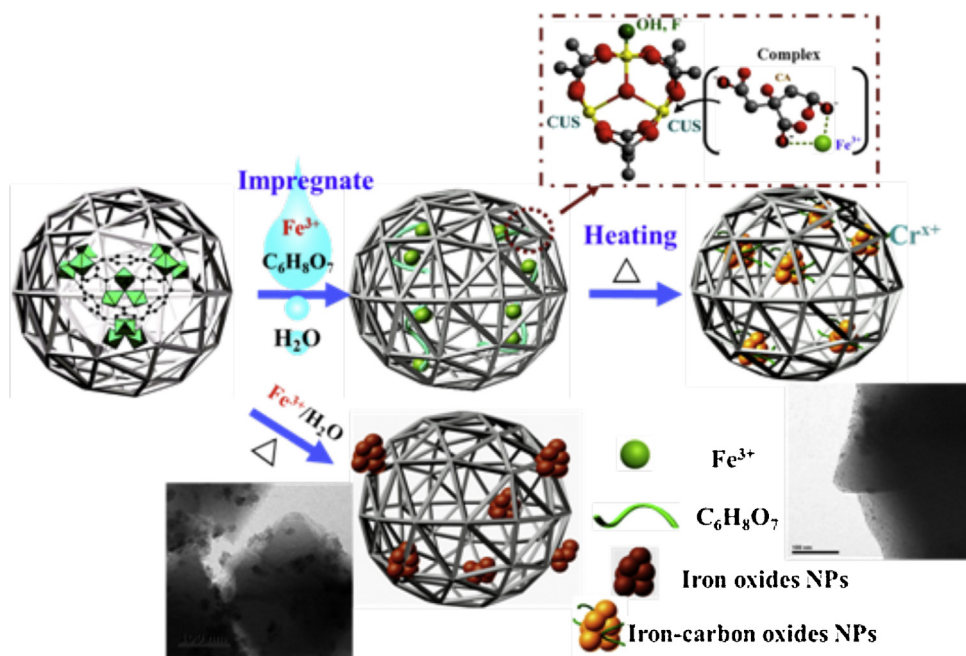
MIL-101(Cr) decorated with  $Fe^{3+}$  ions and tartaric acid (TA) was prepared similar to the synthesis of  $Fe^{3+}$ -CA/MIL-101, and was denoted as  $Fe^{3+}$ -TA/MIL-101(Cr).

#### 2.1.7. $Fe^{3+}$ -CA/MIL-53(Cr), P25, Clay, and meso $NH_2-SiO_2$

The pathways used for fabricating  $Fe^{3+}$ -CA/MIL-53(Cr), P25, Clay, and meso- $SiO_2$  are similar to the synthesis of  $Fe^{3+}$ -CA/MIL-101.

## 2.2. Catalytic experiments

The photocatalytic oxidation of reactive brilliant red X-3B was carried out in a cylindrical Pyrex vessel. In a typical process, a known concentration of catalyst powder ( $0.1 g L^{-1}$ ) was placed in 50 mL of water containing  $100 mg L^{-1}$  of X-3B dye. The initial pH of dye solution was adjusted to neutral value (pH 6.0) by NaOH or  $H_2SO_4$ . Prior to reaction, suspension was stirred continuously in



**Scheme 1.** Preparation of MIL-101(Cr) supporting with Fe–carbon oxides through cooperative organic-acid-directed method with thermal treatment. Impregnating with  $\text{Fe}^{3+}$ –citric acid (CA), a strong interaction between  $\text{Fe}^{3+}$  and CUSs of SBU was established by coordination of carboxylic acid and hydroxyl groups. After heating, in situ growth of Fe–carbon oxides were homogeneously anchored into MOFs. Without CA, most of  $\text{Fe}_2\text{O}_3$  aggregated on out surface of MOFs due to external diffusion of precursor during heating process.

the dark for 30 min to establish the adsorption/desorption equilibrium. All glass vessels were kept at 298 K in a thermostatic water bath oscillator, and the 200 W halogen lamp (emitting radiation: 350–450 nm, maximum emission wavelength: 420 nm) was positioned at the top of the vessel. Catalytic oxidation reaction was initiated by adding a given amount of  $\text{H}_2\text{O}_2$  (1.96 mM) to the solution while the lamp was turned on.

The variation of reactive dye content in samples was determined by U-2910 digital spectrophotometer (Hitachi, Japan) after filtrating by the microfiltration membrane (0.45  $\mu\text{m}$ ). Before the total organic carbon (TOC) analysis, the samples were immediately dealt with the  $\text{Na}_2\text{SO}_3$  (0.15 M) scavenging reagent, and then centrifuged to remove the suspended catalysts. The determination of TOC was carried out on a TOC-V cph analyzer (Shimadzu, Japan). The concentration of ferric and chromic ions in the filtered reaction solution was measured by atomic absorption spectrometer (Varian, USA) equipped with hollow cathode Fe and Cr lamp. The residual  $\text{H}_2\text{O}_2$  concentration during catalytic reaction was analyzed according to the previously reported method [29].

Materials, characterization and other details are shown in Supporting Information (SI).

### 3. Results and discussion

#### 3.1. Catalysts characterization

Surface morphology of the prepared samples was characterized by using SEM and TEM. The typical SEM and TEM images of MIL-101(Cr) show that the crystal presented a good octahedral-like structure and highly oriented growth behavior (Fig. 1a and b). As depicted in Fig. 1c and e, it was clear that the morphology and porous network of MIL-101 host remained intact after loading. Importantly, it was found that the addition of CA prompted the  $\text{Fe}^{3+}$  precursors to be incorporated in the pore of MIL-101(Cr), resulting in the formation of well-dispersed ultrafine NPs encapsulated within the pore of MIL-101 and few NPs deposited on the

external surface (Fig. 1d). By analysis, the chemical formula of Fe–C oxides NPs supported was determined as  $\text{Fe}_{1.06}\text{C}_{0.69}\text{O}_{2.02}$ . However, agglomeration of larger particles existed on the external surface of MIL-101 was observed without the CA adding, and the EDS pattern of attached particles revealed the presence of Fe, Cr, C and O elements (Fig. 1e–f). The results well demonstrated that the addition of CA can greatly enhance the interaction between metal ions and support, and consequently enable the immobilization of Fe–C oxides nanoparticles in the frameworks of MOFs. The size distribution of nanoparticles corresponding to the catalyst  $\text{Fe}^{3+}$ –CA/MIL-101(Cr) and  $\text{Fe}^{3+}$ /MIL-101(Cr) has been explored (Fig. S1 in SI). It was clear that the agglomeration of larger particles existed on the external surface of MIL-101 was observed without the CA adding, and the sizes of NPs ranged from 5.0 to 10.0 nm. In the presence of CA, the diameter of the nanocrystals immobilized to MOFs decreased to less than 4.6 nm, and lots of NPs were found to be much smaller than the pore size of MIL-101.

Fig. 2 shows the elemental mappings of  $\text{Fe}^{3+}$ –CA/MIL-101(Cr) by HAADF-STEM with Fe, Cr, O and C K/L-edges. The typical image in the STEM clearly gives a better morphological understanding of the supported catalyst (Fig. 2a), which demonstrates that Fe–C oxides supported did not destroy the structure of MIL-101. As illustrated by Fig. 2b–f, it is confirmed that a homogenous distribution of Fe can be observed in the supported composite over few monodispersed nanoparticles. Moreover, the results of ICP and EDS analysis for sample  $\text{Fe}^{3+}$ /MIL-101 and  $\text{Fe}^{3+}$ –CA/MIL-101 are presented in Supporting information (Table 1 and Fig. S2). It is clearly indicated that the Fe loading of  $\text{Fe}^{3+}$ –CA/MIL-101 was much three times higher than that of  $\text{Fe}^{3+}$ /MIL-101. This revealed that the organic-acid-directed approach can allow more metal ions to be homogeneously anchored into the channels of MOFs. Consequently, the strategy employed here demonstrated that the adding of functional organic molecules can facilely and effectively control the encapsulation of the NPs into the pores of MOFs and improve the interaction between active sites and the node or ligand of support, which can be easily expanded to other systems.

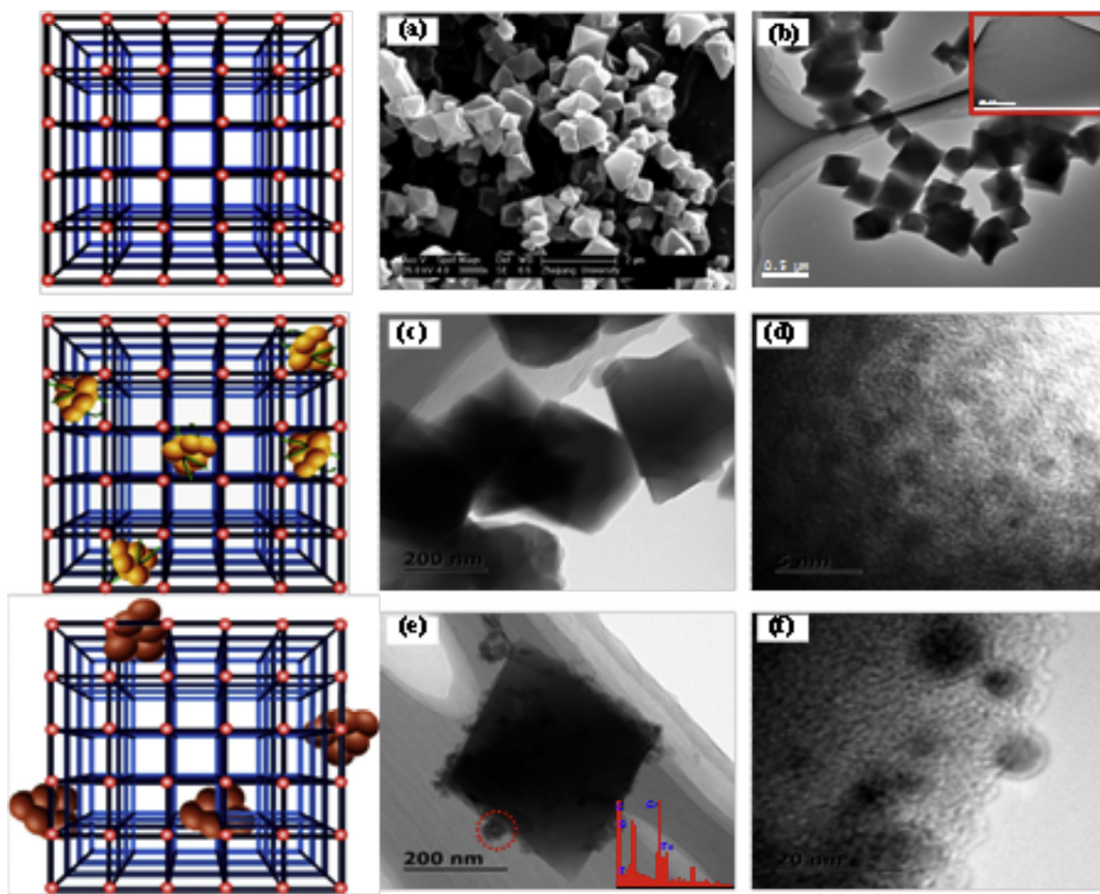


**Fig. 1.** Schematic representation of the MOFs matrix structure before supported (top), after supported by using Fe<sup>3+</sup>-CA solution as precursor (middle), and after supported by using Fe<sup>3+</sup> solution as precursor (bottom). (a) SEM and (b) TEM images of MIL-101(Cr), (c) TEM and (d) HRTEM images of Fe<sup>3+</sup>-CA/MIL-101(Cr), (e) TEM and EDS analysis of Fe<sup>3+</sup>/MIL-101(Cr), (f) HRTEM images of Fe<sup>3+</sup>/MIL-101(Cr).

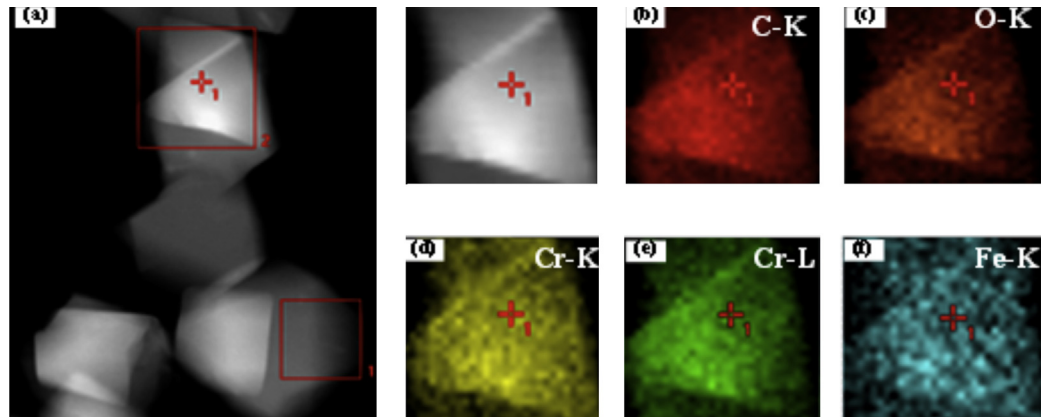


**Fig. 2.** STEM-HAADF image of as synthesized Fe<sup>3+</sup>-CA/MIL-101(Cr) hybrid material (a) and TEM elemental mapping of C, O, Cr, and Fe (b–f).

**Table 1**  
Surface area, textural data and metal compositions for different samples.

Sample	S <sub>BET</sub> (m <sup>2</sup> /g) <sup>a</sup>	V <sub>meso</sub> (cm <sup>3</sup> /g) <sup>b</sup>	Element composition <sup>c</sup> Cr (%)	Fe (%)
MIL-101(Cr)	2561	1.27	17.2	–
MIL-101(Cr)-473K	2207	1.28	17.8	–
Fe <sup>3+</sup> /MIL-101(Cr)	2165	0.87	20.1	0.78
Fe <sup>3+</sup> -CA/MIL-101(Cr)	1116	0.28	16.7	3.86

<sup>a</sup> S<sub>BET</sub> is the BET specific surface area.

<sup>b</sup> V<sub>meso</sub> is the specific mesopore volume obtained from the BJH cumulative specific adsorption volume of pores of 1.70–300.00 nm in diameter.

<sup>c</sup> Analysis of ICP-MS.

The crystalline structures of different samples are presented in Fig. 3. In the diffraction pattern, the distinct well-resolved characteristic peaks of MOFs correspond to the MIL-101(Cr) phase reported by Feírey et al. [26]. After calcinated at 473 K, the MIL-101 crystals also remained unchanged. When decorating with NPs, no apparent loss of crystallinity was appeared for the supported samples, which was similar to the typical XRD diffraction pattern of MIL-101. It indicated that the crystalline structure of the host framework remained intact after loading, consistent with TEM images. However, in comparison with  $\text{Fe}^{3+}$ /MIL-101, it should be noted that the characteristic peaks of sample  $\text{Fe}^{3+}$ -CA/MIL-101 ranged from 8 to 12° were broadened and their intensities decreased dramatically after thermal-treatment, which was mainly attributed to the crystallographic defect since the strong coupling [Fe–O–C] sites with the CUSs of SBU. This also verified that well-dispersed nanoparticles were formed into the lattice of MOFs by the organic-acid-directed method. Moreover, no obvious diffraction was detected for the NPs in XRD pattern of both sample  $\text{Fe}^{3+}$ /MIL-101 and  $\text{Fe}^{3+}$ -CA/MIL-101, deducing the formation of the small particles (Fig. S3 in Si) [21].

Fig. 4 records the FTIR spectrum of different samples. FTIR spectrum of prepared crystal further confirms that it is assigned to the structure of typical MIL-101(Cr) nanomaterials (Fig. 4a). Compared with sample MIL-101-473 K, the spectrum of  $\text{Fe}^{3+}$ /MIL-101 (473 K) remained unchanged (Fig. 4e), which indicated that the supported NPs had a negligible effect on the functional group of MOFs during the traditional impregnating method. It is worth to note that the cross-linking reaction between SBU of MOFs and Fe-CA molecule was evidenced by the FTIR data. After Fe-CA impregnating,  $\text{Fe}^{3+}$ -CA-MIL-101 shows new IR bands at 1554.1 and 1282.4  $\text{cm}^{-1}$  in addition to characteristic MIL-101(Cr) framework vibrations (Fig. 4c), indicating the presence of Fe-CA complex. These bands are slightly shifted to higher wave numbers as compared to the pure ferric citrate (Fig. 4f). However, in the curve of  $\text{Fe}^{3+}$ -CA/MIL-101 (473K), it is evident that carboxylate  $-\text{COO}$ —stretching bands at 1554.1  $\text{cm}^{-1}$  for asymmetric vibration and

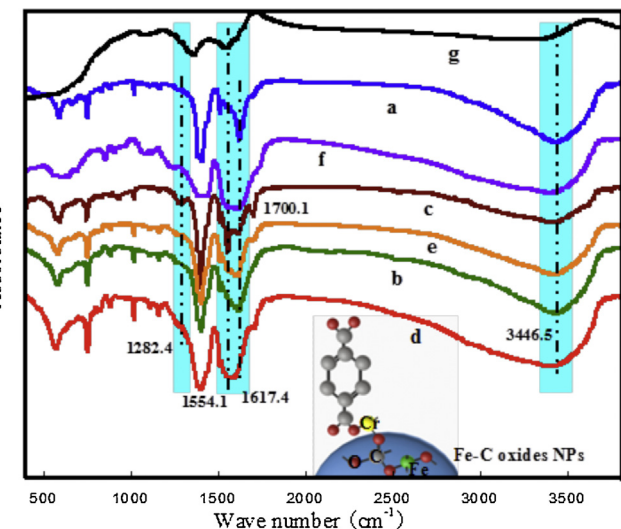


Fig. 4. FTIR spectra of samples MIL-101(Cr) (a), MIL-101-473 K (b),  $\text{Fe}^{3+}$ -CA-MIL-101(Cr) (c),  $\text{Fe}^{3+}$ -CA/MIL-101(Cr) (d),  $\text{Fe}^{3+}$ /MIL-101(Cr) (e), ferric citrate (f), and ferric citrate-473 K (g).

1282.4  $\text{cm}^{-1}$  for symmetric vibration and a  $\text{C}=\text{O}$  stretching band at 1700  $\text{cm}^{-1}$  (both assigned to the metal-organic cross-linker) disappeared, whereas the characteristic peaks at 1617.4  $\text{cm}^{-1}$  shifted slightly to the lower wavenumber and a broad band in the region of 1510–1620  $\text{cm}^{-1}$  appeared (Fig. 4d), which clearly suggests that chemical bond between [Fe–O–C] sites and SBU of MIL-101 has been formed during the thermal treatment (see the inset of Fig. 4). Furthermore, the concentration of chromium (III) CUSs was detected by using FTIR spectroscopy of pyridine adsorption (Py-IR) at low temperature. As shown in Fig. S4, it was obvious that lots of Lewis acidic sites were presented on the sample MIL-101 due to the exposing of unsaturated  $\text{Cr}^{3+}$  sites. After CA impregnating, an obvious decrease in the intensity of Lewis acid center

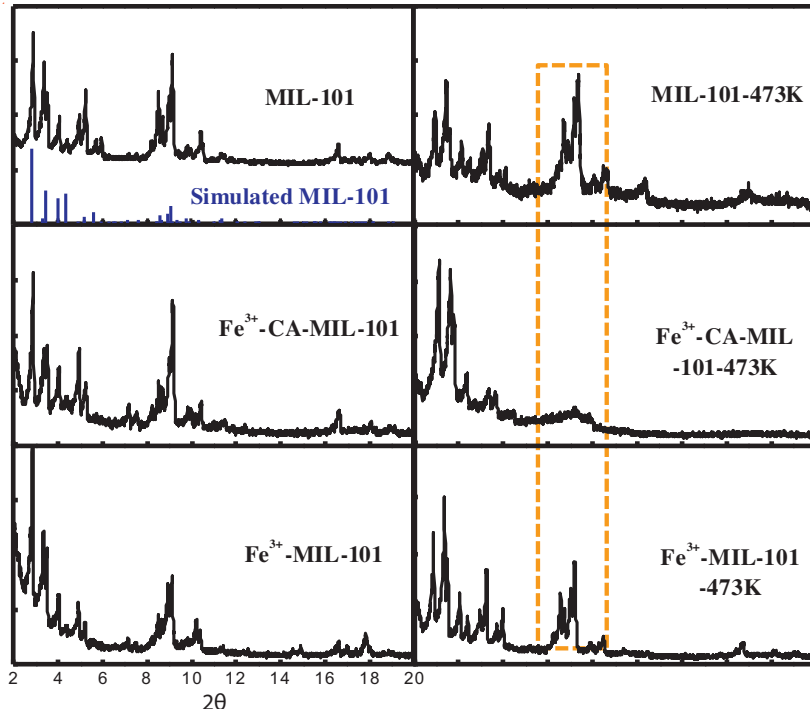
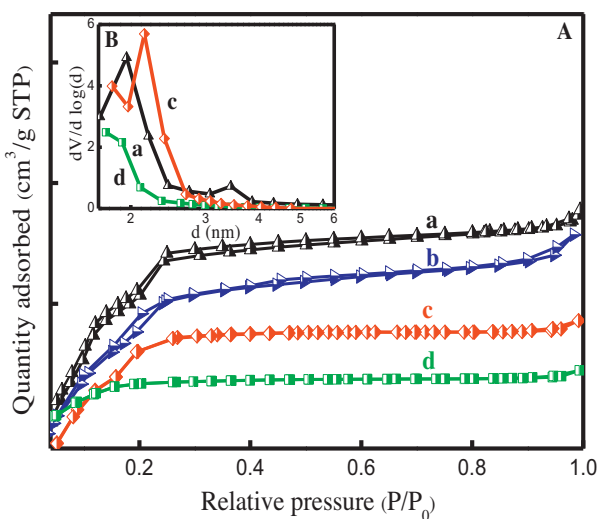


Fig. 3. X-ray diffraction patterns of different prepared samples.



**Fig. 5.** Nitrogen adsorption/desorption isotherms and BJH pore size distribution of (a) MIL-101(Cr); (b) MIL-101–473 K; (c) Fe<sup>3+</sup>/MIL-101(Cr); (d) Fe<sup>3+</sup>-CA/MIL-101(Cr).

characteristic peak (1445 cm<sup>-1</sup>) was observed for sample CA-MIL-101, which clearly indicated that the grafting of CA is coordinated to the chromium (III) CUSs. In comparison with Fe<sup>3+</sup>/MIL-101, a stronger absorption peak at 3446.5 cm<sup>-1</sup> is observed for sample Fe<sup>3+</sup>-CA/MIL-101, which indicates that more dissociative hydroxyl groups are adsorbed on the surface of supported catalyst due to strong hydrophilicity of metal–carbon oxide active sites [30].

Fig. 5 points out the nitrogen adsorption/desorption isotherms and pore size distribution of the prepared catalysts, and the results of the surface area and pore volume are shown in Table 1. As apparent from the figure, the isotherms of MIL-101 displayed an intermediate mode between type I and type IV, which is associated with microporous and mesoporous materials, respectively. The distribution of pore diameter is mainly located in two regions (0–2.5 nm and 3–4 nm). After Fe<sup>3+</sup> and Fe<sup>3+</sup>-CA adsorption, it was apparent that the BET surface area and pore volume of sample MIL-101 decreased (seen from Fig. S5 Table S1 in Si). In comparison with Fe<sup>3+</sup> adsorption (1.18 cm<sup>3</sup>/g), a remarkable reduction in pore volume was obtained for sample Fe<sup>3+</sup>-CA-MIL-101 (0.44 cm<sup>3</sup>/g), which well demonstrated that a large number of Fe<sup>3+</sup>-CA molecule were successfully incorporated into the pore of MIL-101. By the post-modification (thermal treatment), the cavities of the MOFs were occupied with dispersed NPs and/or blocked by NPs locating on the surface.

Compared with sample Fe<sup>3+</sup>/MIL-101, lower surface area and pore volume of Fe<sup>3+</sup>-CA/MIL-101 indicated that more in situ growth of nanoclusters deposited into cavities of the matrix by cooperative organic-acid-directed method. Moreover, the pore size distribution for the supported catalysts presented (see the inset of Fig. 5) that the Fe<sup>3+</sup>/MIL-101 held a larger pore size located between 2 and 3 nm. To investigate the chemical state of NPs supported on MIL-101 through different methods, the XPS measurement of prepared catalysts was carried out and the related results are illustrated in Fig. 6. As shown as XPS spectra, the presence of O1s, Cr2p, F1s, C1s, and Fe2p can be confirmed (Fig. 6a). In the fitting curve of the sample Fe<sup>3+</sup>/MIL-101 (Fig. 6b), the binding energy of the Fe 2p is observed at 712.6 and 726.5 eV, which is assigned to the spectra of Fe 2p<sub>1/2</sub> and Fe 2p<sub>3/2</sub> for the lattice Fe<sup>III</sup>-O in Fe<sub>2</sub>O<sub>3</sub>, respectively [31]. Nevertheless, an obvious shift to lower binding energy for Fe 2p peak was observed for Fe<sup>3+</sup>-CA/MIL-101, indicating no formation of iron oxides [32]. This shift can be ascribed to the formation of Fe–O–C bond in the nanocrystal, which is in agreement with the FTIR results.

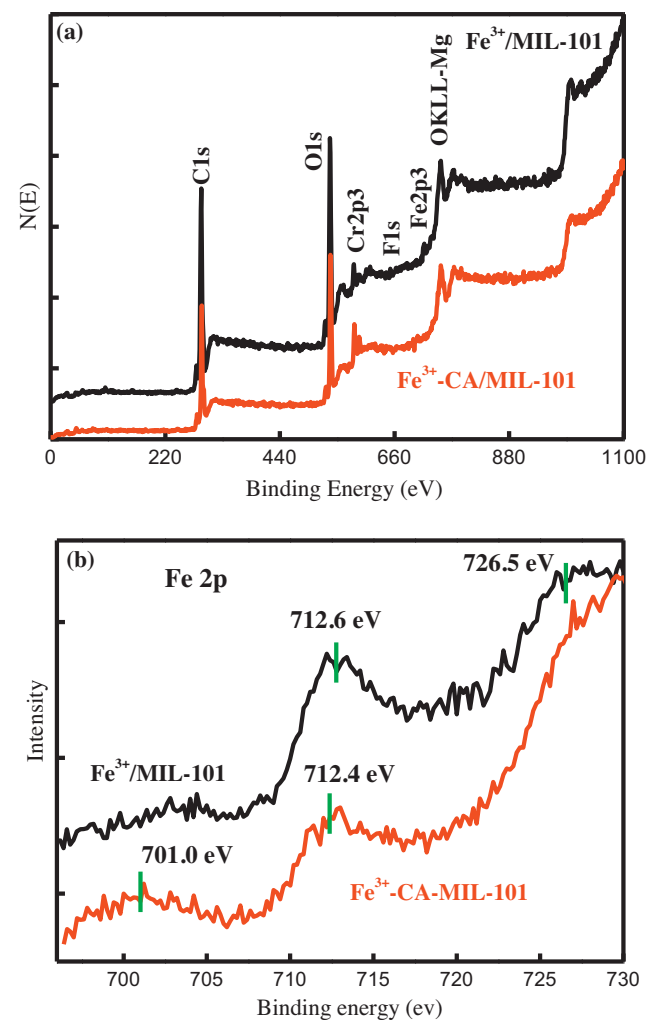


**Fig. 6.** XPS spectra of different samples: (a) full spectra of Fe<sup>3+</sup>/MIL-101(Cr) and Fe<sup>3+</sup>-CA/MIL-101(Cr) and fine XPS spectra of (b) Fe 2p.

### 3.2. Catalytic activity

The photocatalytic oxidation of noxious and refractory organic contaminants in aqueous phase is of great importance in many fields and provides a common way to examine the potential catalytic activity of heterogeneous catalysts. Following most of the previous work, the degradation of reactive brilliant red X-3B to water and CO<sub>2</sub> was selected as model reaction.

Fig. 7 shows the degradation efficiency of dye X-3B by using the different catalytic oxidation processes. Under visible irradiation, the reaction did not proceed by using bare MIL-101 as catalyst, and decolorization was due to the adsorption of solid. In comparison with Fe<sup>3+</sup>/MIL-101, the superior catalytic performance for X-3B degradation was observed in the presence of Fe<sup>3+</sup>-CA/MIL-101 at neutral pH (99.3% photobleaching), but the reactive dyes underwent a slight degradation over pure Fe-A particles (22.4%), which demonstrated that the decomposition of hydrogen peroxide to ·OH radical can be effectively catalyzed by [Fe–O–C] active sites inside MIL-101 support. To illustrate the evidence of ·OH radicals in the catalytic oxidation process, 2-propano has been used as the trapping agent (Fig. S6 in Si). It is apparent that the degradation rate of dye significantly reduced from 99.3 to 50.5% after adding 2-propano, which well indicated that a number of ·OH radicals were generated in the solution and had important effect on the catalytic oxidation of dyes. Refer to the above characteriza-

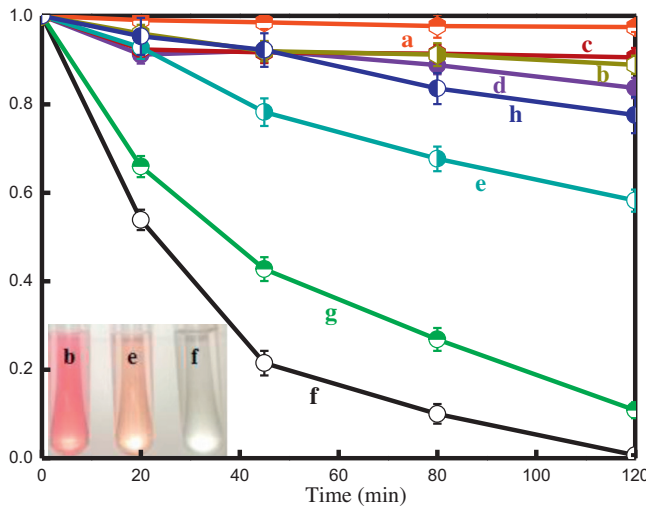


**Fig. 7.** Relative concentration of X-3B as a function of time at different procedure: (a)  $\text{H}_2\text{O}_2$ -light; (b) light-MIL-101- $\text{H}_2\text{O}_2$ ; (c) light- $\text{Fe}^{3+}$ -CA/MIL-101; (d)  $\text{Fe}^{3+}$ -CA/MIL-101- $\text{H}_2\text{O}_2$ ; (e) light- $\text{Fe}^{3+}$ /MIL-101- $\text{H}_2\text{O}_2$ ; (f) light- $\text{Fe}^{3+}$ -CA/MIL-101- $\text{H}_2\text{O}_2$ ; (g) light- $\text{Fe}^{3+}$ -TA/MIL-101- $\text{H}_2\text{O}_2$ ; (h) light-Fe-CA-473K- $\text{H}_2\text{O}_2$ . ( $T = 298$  K,  $C_{\text{cat.}} = 0.1 \text{ g L}^{-1}$ ,  $C_{\text{X-3b}} = 100 \text{ mg L}^{-1}$ ,  $C_{\text{H}_2\text{O}_2,0} = 1.96 \text{ mM}$ , pH 6.0).

tions, the outstanding activity of the catalyst  $\text{Fe}^{3+}$ -CA/MIL-101 in visible-light assisted reaction was accredited to the higher Fe loading, smaller NPs uniformly dispersed into host matrix, and the interaction between the active sites and CUSs of support [33,34]. Meanwhile, a control experiment in the absence of  $\text{H}_2\text{O}_2$  or visible light showed that  $\text{Fe}^{3+}$ -CA/MIL-101 underwent a slight degradation of dyes, and thus proved that cooperative effect of  $\text{H}_2\text{O}_2$  and light irradiation on the performance of catalytic oxidation. Moreover,

similar activity obtained using  $\text{Fe}^{3+}$ -tartaric acid (TA)/MIL-101 as catalyst tended to demonstrate that  $[\text{Fe}-\text{O}-\text{C}]$  catalytic sites were accessible for activation of hydrogen peroxide. By analysis, a similar trend was also found on alteration of XRD and FTIR curves for sample  $\text{Fe}^{3+}$ -TA/MIL-101.

Fig. S7 presents the influence of the Fe loading amount on the catalytic activity of  $\text{Fe}^{3+}$ -CA/MIL-101. It is clear that an obvious increase in the degradation rate of X-3B was obtained from 81.6 to 99.3% with Fe content varying from 5.0 to 10.0 wt%, which was mainly attributed to more Fe-based sites for accelerating the decomposition of  $\text{H}_2\text{O}_2$  to hydroxyl radicals. However, when the loading of ferric ions was further increased to 20.0 wt%, the photo-bleaching rate of dye was decreased to 86.9% and the concentration of leached Fe ion was remarkably increased. It demonstrated that lots of  $\text{Fe}-\text{C}$  oxide NPs could not be immobilized inside the pore of MIL-101. These obtained results clearly indicated that only the  $[\text{Fe}-\text{O}-\text{C}]$  sites bonding with SBU of MIL-101 can play an important role in enhancing the catalytic activity.

### 3.3. Catalyst stability

The stability and durability are important for the practical application of catalysts. After careful washings with methanol and drying, the catalyst  $\text{Fe}^{3+}$ -CA/MIL-101 can be reused in the four successive runs without obvious loss of activity, since more than 94.0% color and 60.0% TOC removal was achieved in 120 min for all runs (Fig. 8a). Leaching test showed that the content of Fe and Cr ions in filtrated catalytic solution remained below 0.08 and 0.01  $\text{mg L}^{-1}$  in all the cycles, which had insignificant influence on the catalytic performance (Fig. S8 in Si). The analysis of XRD and FTIR on the reused catalysts indicated that the crystalline structure and surface properties of MIL-101(Cr) were not damaged after catalytic oxidation reaction (Fig. 8b and c). TEM images pointed out uniform

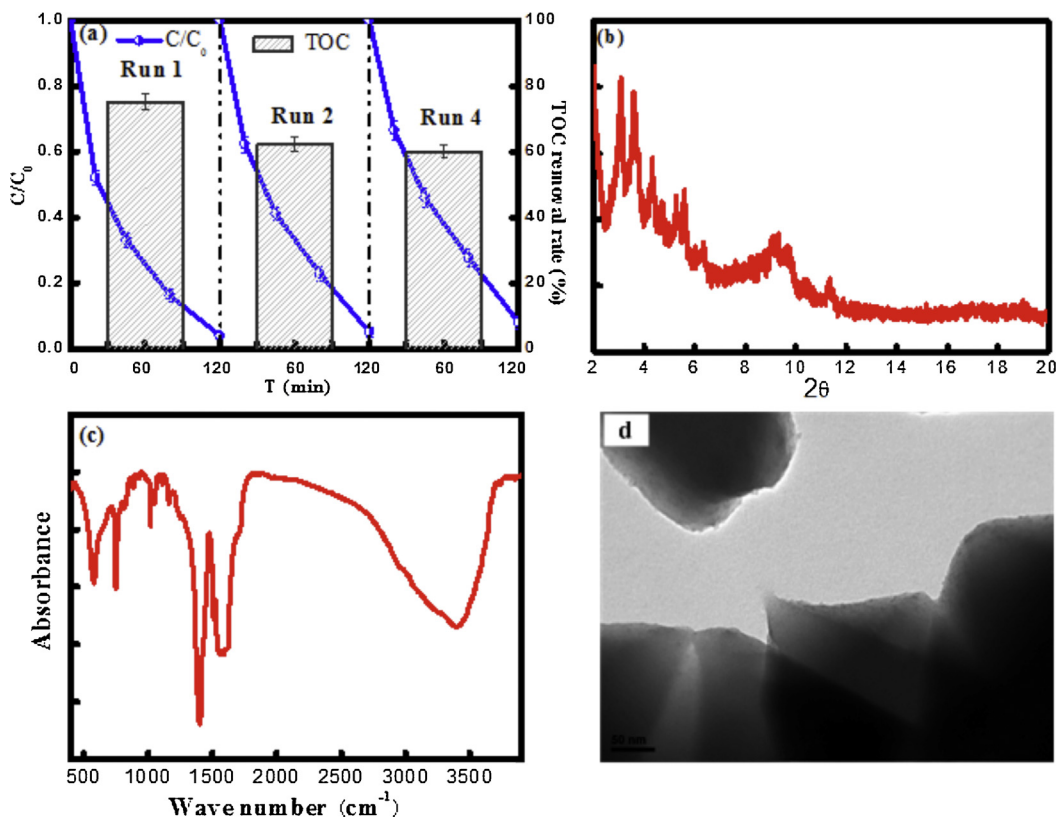
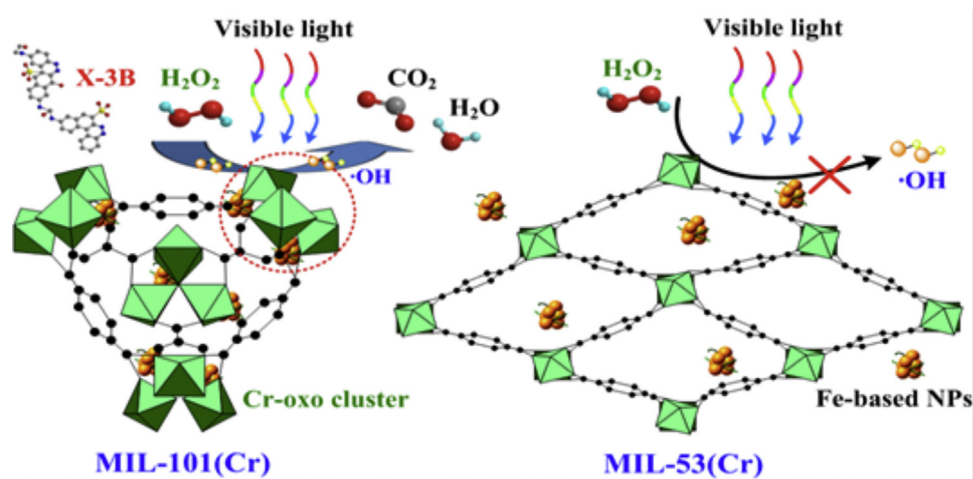


**Fig. 8.** (a) Reusability of the  $\text{Fe-CA/MIL-101}(\text{Cr})$  catalyst after subsequent reactions ( $T = 298$  K,  $C_{\text{cat.}} = 0.1 \text{ g L}^{-1}$ ,  $C_{\text{X-3b}} = 100 \text{ mg L}^{-1}$ ,  $C_{\text{H}_2\text{O}_2,0} = 1.96 \text{ mM}$ , pH 6.0); (b) FTIR, (c) XRD, and (d) TEM investigations of the samples  $\text{Fe}^{3+}$ -CA/MIL-101 reused.



**Scheme 2.** Schematic diagram of MIL-101(Cr) and MIL-53(Cr) supported catalysts for activation of  $\text{H}_2\text{O}_2$  on the catalytic oxidation.

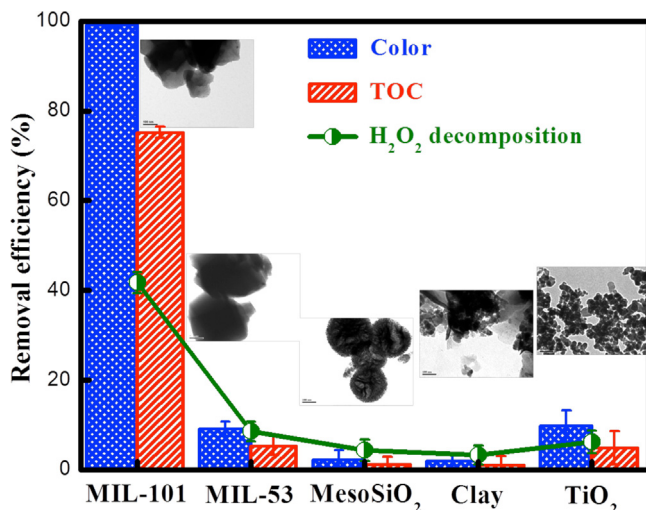


**Fig. 9.** Effect of the different supports decorated with Fe-C oxides NPs on the dye degradation and  $\text{H}_2\text{O}_2$  decomposition.

distribution of NPs without agglomeration after multiple uses in catalysis (Fig. 8d). It confirmed that the  $\text{Fe}^{3+}$ -CA/MIL-101 was stable and resistant to photo-corrosion due to a stable bridge of CA molecule established between the metal ions and SBU of MOFs. This also reveals that the organic-acid-directed approach brings a strong stabilization of ultrafine metal-based nanoparticles well dispersed in the porous frameworks of support.

#### 3.4. Effect of structure and property of support on catalytic activity

In order to better clarify the influence of structure and properties of the support on catalytic performance, we also prepared a series of supported catalysts by organic-acid-directed method and investigated their photocatalytic ability in this study. As depicted in Fig. 9, it is noteworthy that here most of the conventional materials supported catalyst, such as mesoporous  $\text{NH}_2\text{-SiO}_2$ , and  $\text{TiO}_2$  particles, presented low activity for  $\text{H}_2\text{O}_2$  decomposition toward the degradation of dye at low dosage of  $\text{H}_2\text{O}_2$  and catalysts, even if the Fe-C oxide NPs were incorporated into the cavities of supports (TEM images of Fig. S9 in Si). This indicated that high surface area, high porosity, and multi-functionality of MOFs had a significant effect on enhancing the catalytic activity.

Besides, the property-dependence of MOFs materials on the catalytic activity was also highlighted by comparing MIL-101(Cr) with MIL-53(Cr). Interestingly,  $\text{Fe}^{3+}$ -CA/MIL-101 exhibited 10 times more activity than  $\text{Fe}^{3+}$ -CA/MIL-53, in terms of TOC removal and decoloration. Seen from the TEM images of  $\text{Fe}^{3+}$ -CA/MIL-53, it was found that some  $\text{Fe}^{3+}$ -CA molecules were inclined to integrate with MIL-53 depending on weak van der Waals forces and the large Fe-C oxide NPs was generated over the matrix and the external surface of support with a size from 1.0 to 6.5 nm due to the little CUSs exposed (Fig. S10 in Si). As apparent from XRD pattern, the characteristic diffraction peaks and their intensities for sample  $\text{Fe}^{3+}$ -CA/MIL-53 were the same as bare MIL-53 (Fig. S11 in Si), which indicated that no obvious cross-linking reaction between Fe-CA molecule and MIL-53 happened during the preparation. On the basis of this consideration, we therefore proposed the possible mechanism for the activation of  $\text{H}_2\text{O}_2$  by MOFs supported catalysts under visible light irradiation. As illustrated in Scheme 2, the grafting of Fe-C oxide NPs dispersed on outer surface and into cavities of MIL-53 led to a loss of activity due to the detrimental interactions between the NPs and support [35,36]. As reported, the ligand-to-metal charge transfer and metal-oxo cluster excitation had a significant effect on photocatalytic activity of metal-organic frameworks [37,38]. In this regard, it was reasonable to believe that the unexceptionable catalytic properties of MIL-101 supported catalyst were derived from the direct excitation of chromium-oxo cluster and interfacial photo-generated charge transfer between [Fe-O-C] sites and Cr node [39]. This revealed that the synergistic effect of the active sites and metal node of MOFs had a positive effect on catalytic oxidation proceeding. In sharp contrast, it can be concluded that the structure and properties of MIL-101 played a key role in the high activity of WPCHO catalysts with respect to organic matters degradation.

## 4. Conclusions

In conclusion, we have developed a facile and effective approach via cooperative organic-acid-directed method to directly assemble Fe-C oxide NPs on the CUSs of MIL-101(Cr). Compared with traditional solution impregnation, it was found that the organic acid employed can not only lead more ultrafine NPs well-dispersed into the cavities of MIL-101(Cr), but also greatly improve the catalytic activity for activation of  $\text{H}_2\text{O}_2$ . Based on synergistic effect of metal-carbon oxide and metal nodes of MIL-101, its photocatalytic activity was superior than most of the reported conventional supports and MIL-53 (Cr). The present results may offer a new idea for designing green and highly-efficient heterogeneous catalysts by

using MOFs as supports for well-dispersed metal-based NPs, which will be helpful to better understand the correlation between the structure and properties of support and catalytic activity.

## Acknowledgements

This work was supported by the National Natural Science Foundation of China (No. 21236008 and 21476206). Other support includes the Minjiang Scholarship Program from Fujian Provincial Government and Science Foundation Program of Zhejiang University of Technology (No.2014013).

## Appendix A. Supplementary data

Supplementary data associated with this article can be found, in the online version, at <http://dx.doi.org/10.1016/j.apcatb.2015.06.001>

## References

- [1] W.C. Ellis, T.T. Camly, R. Roy, M. Rusten, A. Fischer, D.R. Alexander, B. Blumberg, J.C. Terrence, *J. Am. Chem. Soc.* 132 (2010) 9774–9781.
- [2] T.T. Wu, J.D. Englehardt, *Environ. Sci. Technol.* 46 (2012) 2291–2298.
- [3] R. Gonzalez-Olmos, F.D. Kopinke, K. Mackenzie, A. Georgi, *Environ. Sci. Technol.* 47 (2013) 2353–2360.
- [4] S. Guo, G. Zhang, Y. Guo, J.C. Yu, *Carbon* 60 (2013) 437–444.
- [5] L. Qin, X. Pan, L. Wang, X. Sun, G. Zhang, X. Guo, *Appl. Catal. B* 150–151 (2014) 544–553.
- [6] G. Zhang, L. Qin, Y. Wu, Z. Xu, X. Guo, *Nanoscale* 7 (2015) 1102–1109.
- [7] S. Navalón, R. Martín, M. Alvaro, H. García, *Angew. Chem. Int. Ed.* 49 (2010) 8403–8407.
- [8] N.N. Tušar, M. Maučec, M. Arčon, M. Mazaj, A. Pintar, V. Kaučič, *Adv. Funct. Mater.* 22 (2012) 820–826.
- [9] H. Furukawa, N. Ko, Y.B. Go, N. Aratani, S.B. Choi, E. Choi, A.O. Yazaydin, R.Q. Snurr, M. O'Keeffe, J. Kim, O.M. Yaghi, *Science* 329 (2010) 424–428.
- [10] B. Wang, A.P. Côté, H. Furukawa, M. O'Keeffe, O.M. Yaghi, *Nature* 453 (2008) 207–211.
- [11] L. Ai, C. Zhang, L. Li, J. Jiang, *Appl. Catal. B* 148–149 (2014) 191–200.
- [12] D. Sun, L. Ye, Z. Li, *Appl. Catal. B* 164 (2015) 428–432.
- [13] S. Hermes, M.K. Schroter, R. Schmid, L. Khodeir, M. Muhler, A. Tissler, R.W. Fischer, R.A. Fischer, *Angew. Chem. Int. Ed.* 44 (2005) 6237–6241.
- [14] E.V. Ramos-Fernandez, C. Pieters, B. van der Linden, J. Juan-Alcañiz, P. Serra-Crespo, M.W.G.M. Verhoeven, H. Niemantsverdriet, J. Gascon, F. Kapteijn, *J. Catal.* 289 (2012) 42–52.
- [15] A. Corma, H. García, F.X.L. Xamena, *Chem. Rev.* 110 (2010) 4606–4655.
- [16] J.Y. Ye, C.J. Liu, *Chem. Commun.* 47 (2011) 2167–2169.
- [17] A. Yurderi, M. Bulut, M. Gülcen, Saim Özkar, *Appl. Catal. B* 160–161 (2014) 534–541.
- [18] A.M. Balu, C.S.K. Lin, H. Liu, Y. Li, C. Vargas, R. Luque, *Appl. Catal. A: Gen.* 455 (2013) 261–266.
- [19] H.L. Jiang, B. Liu, T. Akita, M. Haruta, H. Sakurai, Q. Xu, *J. Am. Chem. Soc.* 131 (2009) 11302–11303.
- [20] M.S. El-Shall, V. Abdelsayed, A. El-Rahman, S. Khder, H.M.A. Hassan, H.M. El-Kaderi, T.E. Reich, J. Mater. Chem. 19 (2009) 7625–7631.
- [21] J. Canivet, S. Aguado, Y. Schuurman, D. Farrusseng, *J. Am. Chem. Soc.* 135 (2013) 4195–4198.
- [22] D.Y. Y.K. Hwang, J. Hong, S.H. Chang, Jhung Seo, Y.K. Kim, J. Vimont, A. Daturi, G. Feírey C. Serre, *Angew. Chem. Int. Ed.* 47 (2008) 4144–4148.
- [23] J. Li, Q. Zhu, Q. Xu, *Chem. Commun.* 50 (2014) 5899–5901.
- [24] T.Y. Lin, C.H. Wu, *J. Catal.* 232 (2005) 117–126.
- [25] L.C.A. Ferraz, R. Dallago, L. Conceição, *Catal. Commun.* 8 (2007) 131–134.
- [26] G. Feírey, C. Mellot-Draznieks, C. Serre, F. Millange, J. Dutour, S. Surbleí, I. Margiolaki, *Science* 309 (2005) 2040–2042.
- [27] F. Serre, C. Millange, M. Thouvenot, G. Marsolier, D. Louër, G. Feírey, *J. Am. Chem. Soc.* 124 (2002) 13519–13526.
- [28] J.G. Wang, Q. Xiao, H.J. Zhou, P.C. Sun, D.T. Ding, T.H. Chen, *J. Colloid Interface Sci.* 323 (2008) 332–337.
- [29] J. DeLaat, H.E. Gallard, *Environ. Sci. Technol.* 33 (1999) 2726–2732.
- [30] Y.Q. Liang, Z.D. Cui, S.L. Zhu, Y. Liu, X.J. Yang, *J. Catal.* 278 (2011) 276–287.
- [31] L. Qin, G. Zhang, Z. Fan, Y.J. Wu, X. Guo, M. Liu, *Chem. Eng. J.* 244 (2014) 296–306.
- [32] J. Pola, M.A. Gondal, M. Urbanová, D. Pokorná, H.M. Masoudi, S. Bakardjieva, Z. Bastl, J. Subrt, M.N. Siddiqui, *J. Photoch. Photobio. A* 243 (2012) 33–40.
- [33] T. Ishida, N. Kinoshita, H. Okatsu, T. Akita, T. Takei, M. Haruta, *Angew. Chem. Int. Ed.* 47 (2008) 9265–9269.
- [34] H. Liu, Y. Liu, Y. Li, Z. Tang, H. Jiang, *J. Phys. Chem. C* 114 (2010) 13362–13369.
- [35] J. Joubert, F. Delbecq, P. Sautet, E. Le Roux, M. Taoufik, C. Thieuleux, F. Blanc, C. Copéret, J. Thivolle-Cazat, J.M. Basset, *J. Am. Chem. Soc.* 128 (2006) 9157–9169.
- [36] R.C. Jin, *Nanotechnol. Rev.* 1 (2012) 31–56.
- [37] K.G.M. Laurier, F. Vermoortele, R. Ameloot, D.E. De Vos, J. Hofkens, M.B.J. Roeffaers, *J. Am. Chem. Soc.* 135 (2013) 14488–14491.
- [38] D. Y. Fu, Y. Sun, R. Chen, Z. Huang, X. Ding, Z. Li Fu, *Angew. Chem. Int. Ed.* 51 (2012) 3364–3367.
- [39] K. Meilikhov, D. Yusenko, S. Esken, G. Van Tendeloo, R.A. Fischer, *Eur. J. Inorg. Chem.* (2010) 3701–3714.